(This is a sample cover image for this issue. The actual cover is not yet available at this time.)

Earth and Planetary Science Letters 353–354 (2012) 29–37

Contents lists available at SciVerse ScienceDirect

Earth and Planetary Science Letters

journal homepage: www.elsevier.com/locate/epsl

Complex mantle flow around heterogeneous subducting oceanic plates

Fabio A. Capitanio *, Manuele Faccenda [1]

School of Geosciences, Monash University, Clayton, 3800 VIC, Australia

ARTICLE INFO

Article history:
Received 12 May 2012
Received in revised form
27 July 2012
Accepted 28 July 2012
Editor: Y. Ricard

Keywords:
subduction modeling
mante flow
trench-parallel flow
South American subduction

ABSTRACT

The foundering of oceanic lithospheres controls the circulation patterns of the mantle around subducting slabs. Here, we investigate the sensitivity of the mantle flow to slab buoyancy variations along convergent margins using three-dimensional numerical models of subduction in a viscous mantle. The models illustrate that in a buoyancy-driven system varying subduction velocity arising from negative buoyancy variations effectively drives pressure gradients and confers a general flow component sub-parallel to the margin's strike, allowing for material transport over large distances around the slabs. The along-slab velocity component introduces widespread horizontal simple shear in the mantle flow which is maximized beneath the slab between ~100 and ~350 km. Mantle flow complexities develop rapidly, although not instantaneously, upon subduction of heterogeneous plates. The resulting slab pull gradients are mostly accommodated by internal slab deformation, decoupling the mantle flow from motions at surface. Moderate slab pull variations have a minor impact on plate velocity, and might not result in trench motions, although effectively rearrange the flow. Slab buoyancy heterogeneities are firstly associated with age-dependent thickness variations, but also with slab break offs and windows, varying depth of subduction and entrainment of buoyant blocks. Because these are observed at all subduction zones, the process shown here should have a global relevance for the flow around slabs.

1. Introduction

The negative buoyancy of sinking slabs fundamentally controls the circulation of the mantle around subducting lithosphere. Yet, the complexities of mantle flow and mass transport on Earth remain difficult to constrain from the available indirect observation. Simplified geodynamic models of subduction show that the mantle is entrained with subducting slabs, flowing perpendicular to the trench in both the subslab and mantle wedge, and mass exchange is confined to the slab edges where the flow is mostly toroidal (Funiciello et al., 2004, 2006; Kincaid and Griffiths, 2003; Morra and Regenauer-Lieb, 2006; Schellart, 2004; Stegman et al., 2006). However, the exposed geological analog of the Talkeetna arc, Alaska, shows the occurrence of trench-parallel flow in exhumed mantle wedge rocks, indicated by seismic polarization on horizontal planes (Mehl et al., 2003). Furthermore, isotope geochemistry, seismic velocity anisotropy and attenuation suggest that the flow direction is arc-parallel in the mantle wedge beneath Costa Rica and Nicaragua (Hoernle et al., 2008).

Analytical solutions indicate that lateral gradients in slab properties such as subduction velocity and dip induce similar gradients in pressure (Turcotte and Schubert, 1982), under which the mantle flow may acquire a trench-parallel component (Hall et al., 2000; Kneller and van Keken, 2007). Models of subduction that include realistic slab morphologies, velocity and slab dip variations along the trench (Honda and Yoshida, 2005; Kneller and van Keken, 2007; Morishige and Honda, 2011; Natarov and Conrad, 2012) show some complex patterns of flow, although no trench-parallel and toroidal flow that may reproduce the observations (Hoernle et al., 2008; Rychert et al., 2008) has been found yet.

Observables of subduction velocities and dips at convergent margins show that along-trench variations are common features of subducting slabs (Lallemand et al., 2005), thus suggesting that this mechanism might be of general relevance. In models of buoyancy-driven subduction, variations of subduction rates and dips are firstly related to the balance between the slabs own buoyancy force and plate stiffness and mantle wedge suction (Capitanio and Morra, 2012; Capitanio et al., 2007; Rodríguez-González et al., 2012). Similar buoyancy variations in the subducting lithosphere are primarily due to the age-dependent thickening of plates, so that the observed variations of oceanic plate age along trenches (Müller et al., 2008) must correspond to similar variations in thickness. If so, these should have a role on

* Corresponding author. Tel.: +61 3 99053160.
E-mail address: fabio.capitanio@monash.edu (F.A. Capitanio).
[1] Present address: Department of Geosciences, University of Padua, 35131 Padua, Italy.

0012-821X/$ - see front matter © 2012 Elsevier B.V. All rights reserved.
http://dx.doi.org/10.1016/j.epsl.2012.07.042

the distribution of driving buoyancy force along trenches on Earth, and likely contribute to the organization of circulation patterns at depth.

Here, we use buoyancy-driven subduction modeling to test this mechanism in a subduction system. This approach allows modeling subduction velocities, trench motions, slab dips and mantle flow as emerging self-consistent features of the force balance between slab buoyancy, mantle drag and upper plates resistance (Capitanio et al., 2010b, 2011). Rather than focusing on the role of single parameters, we draw implications for the large-scale dynamics of the coupled lithosphere-mantle system. By modeling heterogeneous buoyancy along the width of subducting slabs, we introduce trench-parallel gradients in subduction rates, trench migrations and dips along the trench and test their impact on flow patterns. In these models, slab pull variations induce sinking rates and pressure lateral gradients introducing a lateral component of the mantle velocity field, perturbing the convective pattern driven by down-going slab. The lateral flow component induces large trench-parallel simple shear strain in a layer at 100–350 km depth, beneath the slabs. Where the trench-ward flow component vanishes, trench-parallel flow occurs, and mass can be transported over large distances around wide slabs. Slabs in the mantle and non-Newtonian mantle flow rearrange readily to minor buoyancy perturbation, although this might not impact plate and trench motions at surface.

2. Modeling strategy, method and setup

Aim of modeling in this work is to test the effect of oceanic plates' buoyancy variation on subduction. The buoyancy of the plate is determined by the density contrast with the mantle integrated over its volume (times gravity). The temperature-dependent density of mantle forming minerals has a primary control on the buoyancy of oceanic lithospheres, modulating the vertical density distribution as well as the thickness of the thermal boundary layer. A detailed analysis of lithospheric mantle density integrated over $h=\sim 105$ km yields average density contrast of $\Delta\rho = 54.3$ kg m^{-3} for a 50 Myr oceanic plate, varying to 28.7 kg m^{-3} for 25 Myr and 63.4 kg m^{-3} for oceanic lithospheres of 90 Myr (Afonso et al., 2007). However, the average density contrast is more likely constant on Earth, $\sim$40 kg m^{-3} (Afonso et al., 2007), whereas the buoyancy varies with the age-dependent thickness of the plate, which scales as $h = 2.32(\kappa t)^{1/2}$, where κ is the thermal diffusivity (Turcotte and Schubert, 1982). For plates of 25, 50, 90 Myr this yields thickness of 65, 92 and 123 km, respectively. Variations of subducting oceanic lithosphere age along the trench are commonly observed (Müller et al., 2008) varying over distances of $O(10^3$ km) (Sdrolias and Müller, 2006), resulting in similar variation of thickness in the subducting slabs. Additionally to this first order buoyancy heterogeneity, oceanic lithospheres host extinct ridges or oceanic plateaux, where lithosphere is locally depleted. Although the integrated buoyancy could vary only by a few percent (Afonso et al., 2007) these can be wide enough to affect the sudbuction, as the Ogasawara Plateau (Miller et al., 2006). Another source of buoyancy heterogeneity during subduction is provided by the entrainment of continental lithosphere segments or blocks. The density and thickness of continental lithosphere vary largely from those of mature oceanic plates, impacting subduction dynamics (Capitanio et al., 2010a). In the subduction models presented here, we use the integrated buoyancy of the plate as a free parameter and discuss later the implications for Earth.

Subduction is modeled as the viscous flow of an infinite Prandtl number fluid at very low Reynolds number in a three-dimensional Cartesian geometry. The flow caused by internal buoyancy is described by the mass and momentum conservation equations:

$$\nabla\cdot\boldsymbol{v} = 0 \tag{1}$$

$$\nabla p - \nabla\cdot\boldsymbol{\tau} = \Delta\rho\boldsymbol{g} \tag{2}$$

where p is the pressure, ρ the density, $\boldsymbol{g}$ the gravity vector, v the velocity and τ is the deviatoric stress tensor:

$$\tau_{ij} = \eta\left(\frac{\partial v_i}{\partial x_j} + \frac{\partial v_j}{\partial x_i}\right) = 2\eta\dot{\varepsilon}_{ij}, \tag{3}$$

where η is the dynamic viscosity and $\dot{\varepsilon}$ is the strain rate tensor. These equations are solved in their non-dimensionalized form with Underworld, a Lagrangian integration point finite element method, in a 3D Eulerian grid (Moresi et al., 2003). The details of the numerical method, software implementation and relevant numerical benchmarks are described in Moresi et al. (2003) and Stegman et al. (2006). The numerical resolution of the models is $96\times96\times64$, in the x, y, z directions respectively.

The model space is a 3D Cartesian box, 4000 km long, 8000 km wide and 1000 km deep, and is derived from Capitanio et al. (2011). The boundary conditions are periodic on the front and rear walls (x=0, 4000 km), free-slip on top and sidewalls, no-slip on the bottom and a symmetry plane in y=0 (Supplementary Fig. 1). For the symmetry adopted only half model space is modeled, i.e. y [0, 4000 km]. We neglect the role of the Earth's sphericity since it has a negligible role on the subduction dynamics (Morra et al., 2006), and does not affect the pressure gradients addressed. The subducting lithosphere is 6000 km wide and is a Newtonian body, with a strong, 10^{23} Pa s, 70 km thick top layer, and a 10^{21} Pa s, 30 km thick bottom layer, with an additional Byerlee's plasticity law in the top 30 km:

$$\tau_Y = \tau_0 + \mu p, \tag{4}$$

where τ_0=35 MPa is the cohesion, μ=0.01 the friction coefficient, in agreement with commonly used values (Krien and Fleitout, 2008; Sobolev and Babeyko, 2005). The subducting plate-mantle density contrast chosen is $\Delta\rho$=53 kg m^{-3} compatible with realistic buoyancy estimates (Afonso et al., 2007). The model's upper plate has no density contrast with the mantle, a thickness of 40 km and Newtonian viscosity of 10^{24} Pa s, reducing the trench curvature to a minimum (Supplementary Table 1). An incipient slab, extending to 150 km depth initiates subduction, after which it is self-sustaining.

The upper mantle viscosity is

$$\eta_M = \eta_0\left(\frac{\dot{\varepsilon}_{\mathrm{II}}}{\dot{\varepsilon}_{\mathrm{II}_0}}\right)^{1-n/n}, \tag{5}$$

where $\dot{\varepsilon}_{\mathrm{II}} = \sqrt{\dot{\varepsilon}_{ij}\dot{\varepsilon}_{ij}/2}$ is the second invariant of the strain rate tensor, and $\dot{\varepsilon}_{\mathrm{II}_0}$ the reference strain rate. Every model has been run with values of n=1 and $\eta_0 = 2\times10^{20}$ Pa s, i.e. Newtonian mantle, and n=3.5 and $\eta_0 = 2\times10^{18}$ Pa s, i.e. non-Newtonian mantle (Suppl. Table 1). A linear viscosity of 10^{21} Pa s is imposed below 660 km depth, and a density increase of 50 kg m^{-3} (Suppl. Fig. 2).

The models run to steady state subduction of a reference model with constant buoyancy slab and Newtonian mantle (that is more computationally efficient), then the model is perturbed. The models enter a steady state after the slab has reached the transition zone, i.e. 660 km have been subducted, and lasts throughout the final stages of the subduction, until the unsubducted plate has reduced to $\sim$800 km. Slab and mantle velocities and slab morphology are constant throughout the steady state.

The distribution of plate buoyancy along the trench direction is the free parameter in our models. We have modeled it testing three different buoyancy perturbations, that is varying the thickness throughout the slab length l (Suppl. Fig. 1, Suppl. Table 1,

Models 1–11), varying the density contrast (Mods. 12–19) and varying the thickness of a smaller length m (Mods. 20–21).

The thickness is varied by changing the rheology of the plates lowermost 30 km to that of the mantle. The rheology is changed in the outer portion of the slab width, and is viscous (i.e., Newtonian), 100 km thick in the center of the slab of width d (Suppl. Fig. 1), modeled values of d are 100, 500, 200 km. In a second setup we tested the role of a smaller length of plate of varying thickness m to model self consistently the entrainment of buoyancy heterogeneities. Finally, we tested the variation of buoyancy keeping the thickness constant along the slab and changing the density contrast (Suppl. Table 1). All models are run with both a Newtonian and a non-Newtonian mantle.

After the perturbation the models run until the lithosphere is entirely subducted. The measurement used for comparisons are conducted 2–3 Myr after the slab is perturbed, this is the time required to rearrange the flow.

Measured quantities are the pressure, where in the remainder of this paper we refer to the dynamic (i.e. non-hydrostatic) pressure, velocity and shear stress. To characterize the flow we measure the vorticity, i.e. the curl of the velocity:

$$\omega = \nabla \times v \tag{6}$$

Finally, we measure the dissipation partitioning and provide an estimate of the dissipation in the lithosphere over the total:

$$\Phi_L = \frac{\int_L \tau_{ij}\dot{\varepsilon}_{ij} dV}{\int \tau_{ij}\dot{\varepsilon}_{ij} dV}, \tag{7}$$

where L is the lithosphere volume. The lithospheric dissipation is integrated in the volume of the plate where the viscosity has not been decreased by plasticity, that is the shear zone at the trench is not considered part of the subducting plate.

3. Results

3.1. The effect of buoyancy variations

We first compare the model where the buoyancy is constant along the slab with the varying buoyancy model, with $d=2000$ km (Fig. 1, Suppl. Table 1, Mods. 8 and 11). Large buoyancy in the subducting plate center drives faster subduction locally (Fig. 1A and D). The slab accommodates the differential motions at depth through internal deformation. Yet, the differences in trench motions are negligible in these models, and trenches remain straight due to the high viscosity of the upper plate. The trench-ward velocity component, v_x, measured at the models' surface, $z=0$, and $y=1000$ km, differs due to the average buoyancy increase, 4 and 6 cm yr^{-1} in constant and perturbed buoyancy models, respectively. However the flow pattern is in general very similar (Fig. 1B and E), forming a convective cell sustained by the downgoing slabs and a vigorous return flow. The component of the velocity v_y that is perpendicular to the cross-section plane xz is negligible when the slab model has a constant buoyancy (Fig. 1C), instead it is larger in the models where slab buoyancy varies laterally (Fig. 1F). In this model a broad area beneath the slab extending for ~400 km from the slab where the velocity v_y is between 1 and 3 cm yr^{-1}.

The viscosity profile beneath the subducting plate (Suppl. Fig. S2A) is very similar for both models, reaching $\sim 7\times10^{19}$ Pa s in the asthenosphere, beneath the plate and slightly increasing to

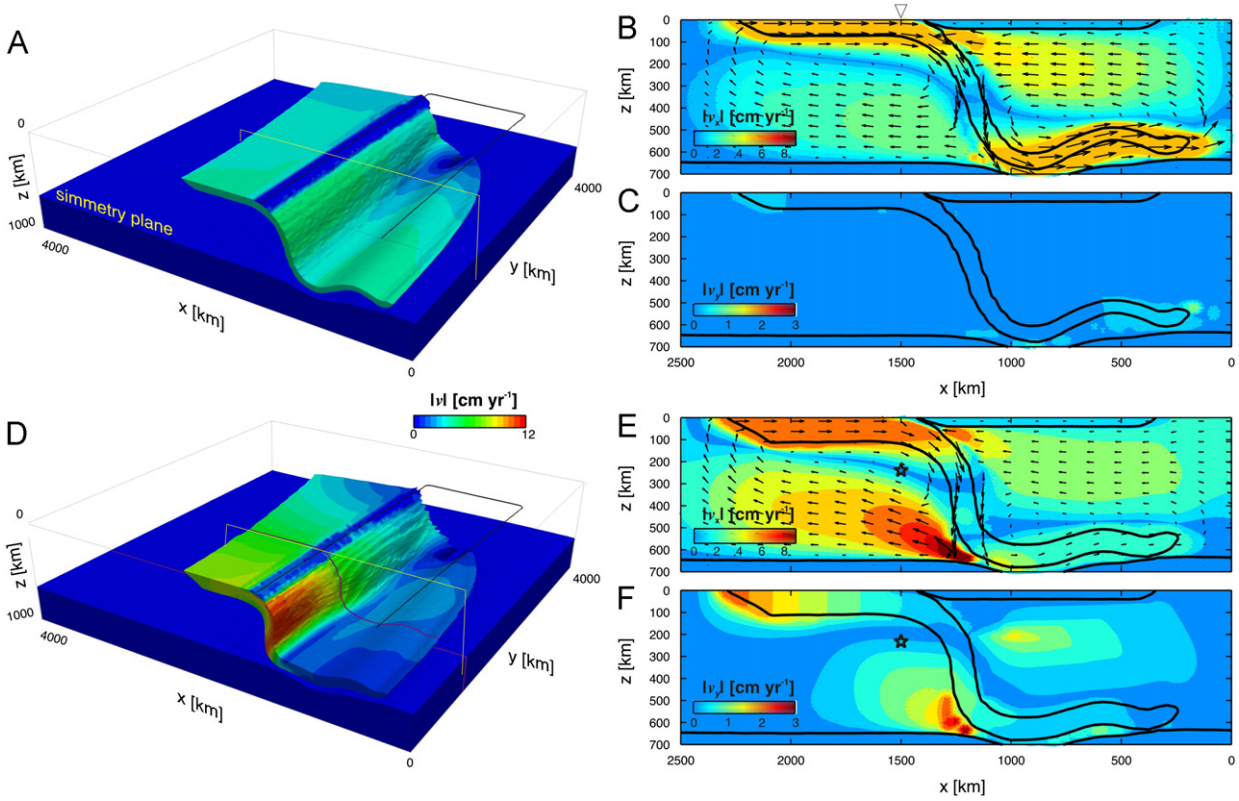

Fig. 1. Homogeneous vs. heterogeneous models with non-Newtonian mantle. Constant thickness Mod. 8 (A, B, C) and variable thickness Mod. 11 (D, E, F) models at the steady-state, contour of the density field with velocity magnitude in color. Black line on top, trace of the upper plate. Thick purple line in D the location of the thickness boundary. In yellow (A, D) the trace of the cross sections. Sections are taken at $y=980$ km. (B, E) Horizontal velocity component magnitude, v_x, and velocity vectors. (C, F) Velocity component perpendicular to the section plane, v_y. Density contour in black line. Star symbol in E, F location of symbol in Fig. 2. (For interpretation of the references to color in this figure legend, the reader is referred to the web version of this article.)

mid-mantle depth, and decreasing at the bottom of the upper mantle at ~660 km depth. The component v_y in the cross-section plane is negligible when slab buoyancy is constant and it is as high as 2–3 cm yr^{-1} when slab buoyancy varies along this direction. In a vertical profile of the normalized velocity (Fig. 2) we show the component v_y is around a third of the v_x component in heterogeneous buoyancy models throughout the upper mantle thickness, and is negligible in the constant buoyancy models. Largest v_y are found between 300 and 550 km depth, although the whole upper mantle flow is characterized by a lateral velocity component.

A depth at which the component v_x is zero is found at ~200 km. In this ~30 km thick layer, although the flow velocity is low, the trench-parallel flow is dominant (Fig. 2). The location of this point (Fig. 1E and F, star symbol) coincides with the location where flow sheared by the plate reverts to the return flow found deeper, and velocity in this plane is zero, i.e. no horizontal or vertical motions. Yet, the lateral component is non-zero, so that the lateral transport in this layer is maximized. In the plane at this depth pressures of ~2 MPa occur beneath the homogeneous slab, decreasing only at ~1000 km from the slab edge (Fig. 3A). Above the slab, in the mantle wedge, a broad low pressure extends all along the slab, where pressure is ~ −9 MPa. The flow beneath the slab follows the pressure field, thus circulation is mostly perpendicular to the trench, except near the slab edge, where toroidal flow develops. The along-trench velocity, v_y, is almost negligible around the slabs center, and is only large close to slab edges, when it has constant thickness. The path of particles immersed in the velocity field in this plane (Fig. 3B) shows that the mass exchange between the mantle wedge and below the slab is limited to ~1000 km from the slab edge, whereas particles beneath the slab follow the trench-perpendicular path. Instead, in the model that includes plate's buoyancy heterogeneity, the flow is more complex and has a stronger trench-parallel component (Fig. 3C). The thicker, more negatively buoyant slab segment induces larger subduction velocity locally and a strong pressure gradient along the slab. When slab thickness varies along the slab, the trench-parallel velocity v_y component is largest around the thickness variation (Fig. 3D). The dynamic pressure gradient above the slab is larger, and results in faster flow towards the center of the slab. The path of the particles immersed in this flow shows that mass from beneath the center of the slab can be transported along the trench-parallel direction to the slab edge, and from there is entrained in the mantle wedge and reach as far as the center of the 6000 km wide slab. In models where the slab has constant thickness, the vorticity is large only around the slab edge (Suppl. Fig. S3A). Instead, when the slab

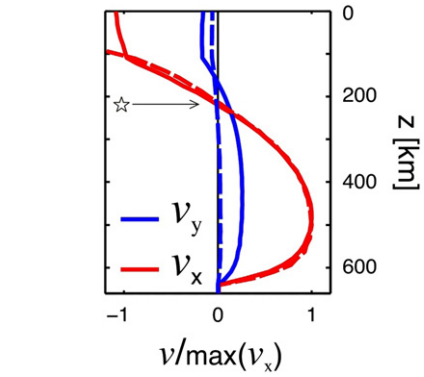

Fig. 2. Normalized velocity vertical profiles from the two models in Fig. 1. Location of the section is indicated in Fig. 1B by the star. Dashed lines, model in Fig. 1A (Constant thickness slab), solid lines model in Fig. 1D (Variable thickness slab).

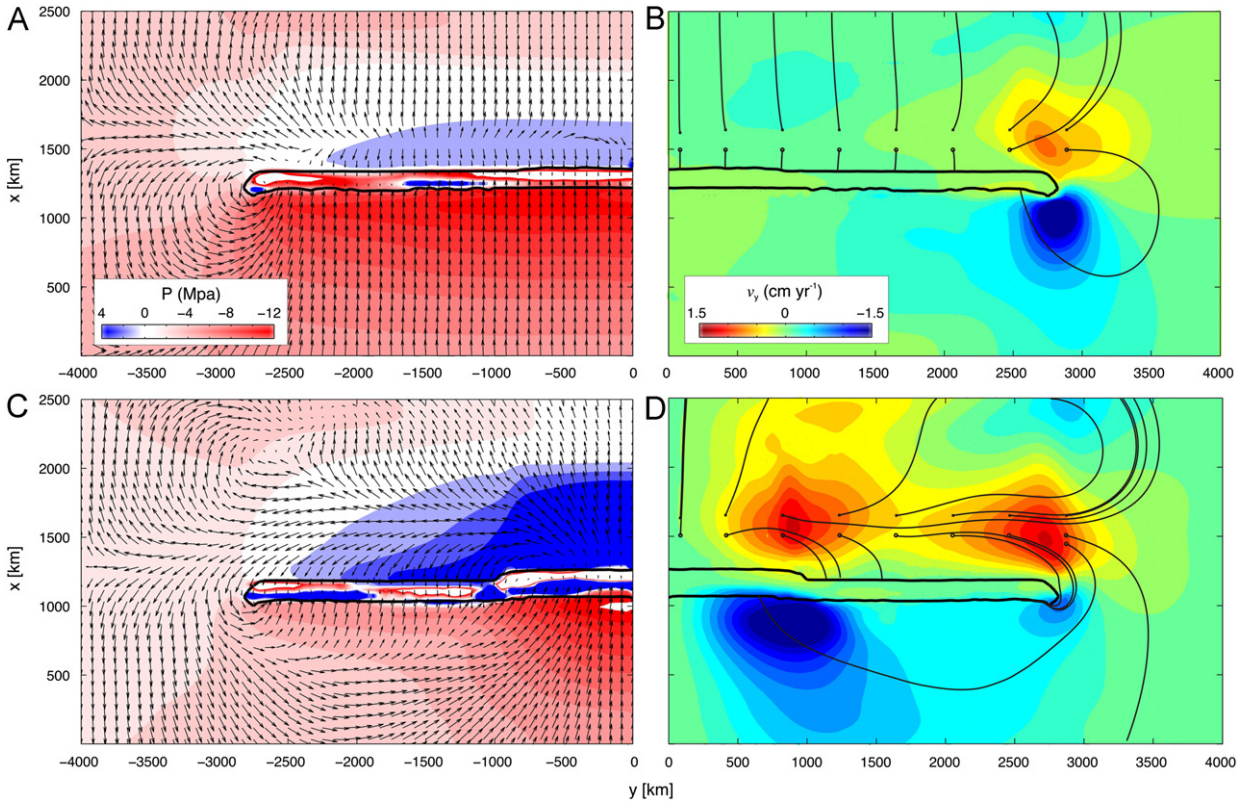

Fig. 3. Detail of the horizontal (half) section through the models in Fig. 1. Depth of the sections is ~200 km, indicated by star symbol in Fig. 2. Density contour in black line. Dynamic pressure and velocity vectors of constant (homogeneous, A) and variable thickness (heterogeneous) models (C) with non-Newtonian mantle rheology. Velocity arrows are not scaled. Lateral velocity v_y and streak lines of particles indicated by small circle symbols.

buoyancy varies laterally, the magnitude of the vorticity is larger overall, since it is large around the internally deforming slab (Suppl. Fig. S3B).

To better characterize the deformation in these models, we have calculated the ratio:

$$r = \left(\frac{\partial v_y}{\partial x} + \frac{\partial v_y}{\partial z}\right) / \left(\frac{\partial v_x}{\partial y} + \frac{\partial v_x}{\partial z}\right) \quad (8)$$

indicating the ratio between the components of the velocity gradient defining simple shear in the y direction over that in the x direction. For the straight morphology of the slab model we refer to the ratio of trench-parallel to trench-perpendicular simple shear. Simple shear in constant slab buoyancy models is negligible around subducting plates (Fig. 4A), it only increases around the slab edges. This results in very low values of r. Instead, in slabs of variable thickness values of $r \sim 1$ are widespread in the whole modeled upper mantle domain, indicating that (1) the components of the simple shear are comparable, and (2) this is a general characteristic of the flow. In this model, values of r are larger beneath the slab between 100 and ~350 km depth (Fig. 4B), in an area ~200 km wide, found beneath the trench in our models. In this area trench-parallel simple shear is maximized, and in average $r > 2$, reaching values of ~8–9 closer to the slab, so the trench-parallel simple shear is up to 8–9 times larger than the trench-perpendicular component. Large values of r are found beneath the upper plates in these models, however, this is possibly the result of the very high viscosity in the topmost layers, resulting in steep unrealistic velocity gradients.

3.2. Sensitivity of mantle flow to buoyancy perturbations

In Fig. 5 we summarize the results of the models 8 to 11, where we have varied the thicker segment width, d. Measures are taken from a plane beneath the slabs, at 450 km depth, where the flow velocity is maximized. The dynamic pressures measured vary from 1.9 MPa in the center of constant thickness slab to 3.8 MPa beneath the model with $d = 2000$ km. For d smaller than 2000 km, the maximum pressure decreases, despite the buoyancy in this area being the same. Gradients across the thickness variation are smooth compared to the step-like buoyancy change. The subduction velocity measured at depth, v_{sub} (the magnitude of the flow velocity, outside the slab) varies along the width of the slab, with the maximum achieved in the center, where the buoyancy is increased. Here, velocity ranges from 5 to ~12.5 cm yr^{-1}, from constant to varying buoyancy slabs with $d = 2000$ km. Similar to pressure gradients, velocity varies smoothly along the slab. Although the subduction velocity in these models depends in the first place on the slab buoyancy (Capitanio et al., 2007), the velocity gradients along the slab depend also on their stiffness, when their viscosity is finite. The stiffness controls the propagation length of the buoyancy perturbation through the wavelength $L = 2\pi h(\gamma/6)^{1/3}$ (Turcotte and Schubert, 1982), where γ is the lithosphere/mantle viscosity contrast and h the thickness of the lithosphere. In our models $\gamma \sim 10^4$ in the $h \sim 30$ km thick lithospheric core, yielding $L \sim 2200$ km, and $L/2$ is the distance from the step in thickness where differences between models become small (Suppl. Fig. S4A). Although simplified, this explains why only models where buoyancy anomaly is $d \sim L$ achieve a full subduction velocity, whereas it is lower in models with $d \ll L$, despite their buoyancy in the center being the same. Because the torque in the mantle is applied on the plane containing the slab thickness h, slabs accommodate sinking rate gradients, bending, readjusting dip or migrating, resisted by a force $\propto h$. Instead, at plate margins the torque, resulting from slab pull gradients applied on plane to the plates' width, has a larger resistance to deformation. This explains why gradients in models' surface velocity are small (Fig. 5B, thin lines).

Trench-parallel velocity of the mantle beneath the slabs is negligible when models' buoyancy is constant, and increases with increasing d, reaching the same velocity of the toroidal flow around the edges in models with $d = 2000$ km (Fig. 5C). We explain it as the result of the subduction velocity gradients. The pressure p beneath a slab of velocity v_{sub} is (Stevenson and Turner, 1977), that is the Couette flow:

$$p = \frac{2a\eta v_{sub}}{r}, \quad (9)$$

where $a = \sin\alpha/[(\pi-\alpha)+\sin\alpha]$ with α being the slab dip and η is the fluid mantle viscosity and r is the downward distance along the slab. Assuming that (1) the dip angle and, (2) the viscosity variations along the slab are negligible, i.e. $\partial a/\partial y = 0$ and $\partial\eta/\partial y = 0$,

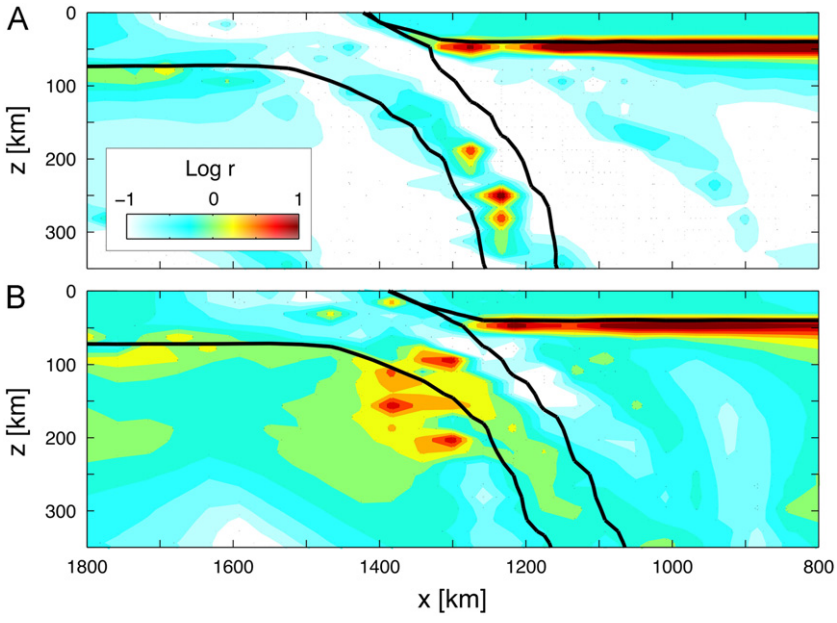

Fig. 4. Ratio r, Eq. (8), of trench-parallel to trench-perpendicular simple shear in constant (A) and variable thickness (B) models with non-Newtonian mantle (Fig. 1). The cross section are taken at $y = 1080$ km.

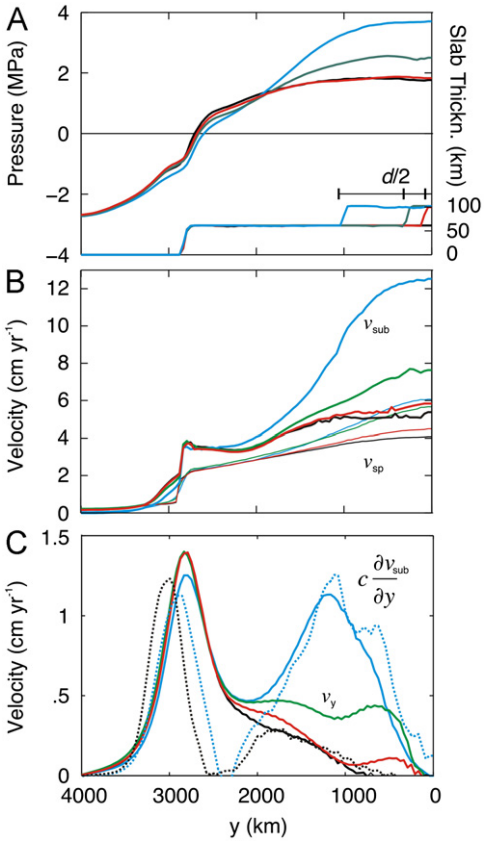

Fig. 5. Comparisons of models with thickness variation along the slab width with non-Newtonian mantle rheology. Constant thickness model mod. 8 black lines, mod. 9 in red, mod. 10 in green and mod. 11 in light blue. Depth of section indicated by star symbol in Fig. 2. (A) Pressure distribution in the subslab and thickness variation along the slab width. (B) Subduction velocity in the slab (thick lines) and velocity at the surface v_{sp} (thin lines). (C) Lateral velocity component v_y (solid lines) increases with d and recovered velocity (dotted lines). (For interpretation of the references to color in this figure legend, the reader is referred to the web version of this article.)

and (3) we use (9) which is for an infinitely wide plate, the pressure gradient in the direction y, perpendicular to the plane xz, that is

$$\frac{\partial p}{\partial y} = \frac{\partial p}{\partial v_{sub}}\frac{\partial v_{sub}}{\partial y} = \frac{2a\eta}{r}\frac{\partial v_{sub}}{\partial y} \tag{10}$$

The pressure gradient $\partial p/\partial y$ induces a flow of maximum velocity v_y, i.e. the Poiseuille flow, in an incompressible fluid of viscosity η in a channel of height H this is (Turcotte and Schubert, 1982):

$$v_y = -\frac{H^2}{8\eta}\frac{\partial p}{\partial y} \tag{11}$$

where we consider the velocity $v_y=0$ at the slab surface. Substituting (10) in (11):

$$v_y = -\frac{aH^2}{4r}\frac{\partial v_{sub}}{\partial y} = b\frac{\partial v_{sub}}{\partial y}, \tag{12}$$

showing that mantle flow component v_y develops as a result of gradients in the subduction velocity. The lateral component of the velocity is independent of the fluid viscosity (Hall et al., 2000). Taking $r=(450-h)/\sin\alpha=372$ km, where $\alpha=70^\circ$ is the average dipping angle and $H=560$ km is the subslab upper mantle, Eq. (12) recovers comparable trench-parallel velocities beneath the slab (Fig. 5C, dotted lines), introducing a fitting constant $c=2b$, despite the simplification assumed. This offers a rule of thumb to understand the lateral flow component from the gradients of subduction velocities at depth.

While this analysis holds for Newtonian mantle models as well, where the characteristics of the flow are the same, introducing non-linearity in the mantle rheology affects the gradients of strain patterns, i.e. strain rates. In the models, simple shear accommodates the differential motions between the slab, where $v_y\sim0$, and the flow of largest v_y, at $\sim$300 km from the slab in the plane of the section. To illustrate this, we show the scaling of simple shear strain rates $\dot{\varepsilon}_{xy}$ beneath the slab with the magnitude of the velocity v_y (Suppl. Fig. S4B).

The dissipation partitioning in these models is similar, increasing from $\Phi_L=11\pm5\%$, in the constant buoyancy model, to $\Phi_L=17\pm4\%$ in the model with $d=2000$ km. This shows that the mantle drag force is very weakly dependent of the circulation pattern.

4. Discussion

4.1. Comparison with previous studies and implications

Many studies have addressed the mantle flow associated with subduction presenting two- and three-dimensional numerical and laboratory models. While a review of these is not the aim of this paper, we will focus here on the new perspective our approach introduces.

Global models of subduction and mantle convection have explained the pattern of plate motions, mantle flow and its alignment with seismic anisotropy (Becker et al., 2003; Conrad et al., 2007; Natarov and Conrad, 2012). These models derive the large-scale buoyancy distribution of the mantle from tomographic models, which account appropriately for the first-order dynamics. However, these models do not capture the smaller scale complexities of the flow around subduction zones.

Thus so far, only models where a realistic morphology of the subduction zone has been considered can explain the complexities of the flow in the mantle wedge (Billen et al., 2003; Jadamec and Billen, 2010; Kneller and van Keken, 2007) or as a global feature (Natarov and Conrad, 2012). While they illustrate accurately the role of local complications in the mantle flow, making inferences on a general flow mechanism from this approach remains difficult.

The approach to buoyancy-driven subduction allows modeling several of these relevant aspects at a glance, offering insight into the fundamental mechanisms that relate motions and deformations in the mantle and plate. Variable buoyancy of plates result in a range of subduction parameters including sinking velocity, slab dip and radius, which are interdependent (Capitanio and Morra, 2012; Capitanio et al., 2007). In a realistic three-dimensional setting, where these heterogeneities are present the resulting velocity and dip variations confer morphologies similar to the observed as well as realistic continental tectonics (Capitanio et al., 2011). Here we have shown that these heterogeneities also account for complex mantle flow around slabs.

Other subduction zone regional features have the power to modify the subduction parameters, such as the friction at the plate margins (Iaffaldano et al., 2012) or the suction of upper plates (Rodríguez-González et al., 2012). However, these effects act at shallow depths and cannot alter the overall sinking dynamics (Capitanio and Morra, 2012; Capitanio et al., 2010b; Dvorkin et al., 1993).

Along-trench buoyancy variations are required to explain complex slab morphologies (Capitanio et al., 2011) and flow around slabs, but also might potentially reduce the misfit between predicted and observed global plate motions. In fact,

the overall mantle flow in our models is very similar to the 2D flow usually reproduced by subduction models (e.g. Garfunkel et al., 1986), where a convecting cell follows the downgoing motions of the slabs. This is because the buoyancy perturbations introduced are small enough that the fundamental dynamics is not changed. Global models of plate motions in fact allow small corrections to the global plate motions circuit, which have a rather regional character (Kreemer, 2009; Stadler et al., 2010). Although varying rheology might act to decouple plate motions and slabs (Jadamec and Billen, 2010) to improve the fit between observed and predicted motions (Stadler et al., 2010), these still have a "regional" extension. Here, we suggest that the fit in plate motions might be improved by considering the buoyancy structure of subducted slabs, rather than assuming constant thicknesses. This introduces realistic driving force gradients, and possibly local variation to resisting forces could be less relevant.

4.2. Subduction motions, mantle flow and seismic anisotropy

Our modeling results indicate that the structure of the non-Newtonian mantle flow is very sensitive to the slab buoyancy configuration, developing lateral flow rapidly. Yet, the relation between mantle flow and surface plate motions is non-unique. When stiff upper plates override subducting plates, the relative motions of the slab are hampered, as seen here. Furthermore, coupling gradients along the shear zone between plates might also result in forced trench and slab motions at depth (Capitanio et al., 2011; Iaffaldano et al., 2012). Here, we have shown that in both cases the mantle flow at depth responds only to the buoyancy structure of the slab at depth. This can be understood by considering that the buoyancy structure confers slab pull gradients, which can be accommodated within slabs by internal deformations, thus stresses are not propagated to the trench. This is the opposite case in models treating the slabs as infinitely rigid (Buttles and Olson, 1998; Hall et al., 2000), where the slab motions at depth are strongly coupled with the plate and trench motions at surface. Internal slab deformation as in the models presented here is compatible with the complex morphology of the slabs seen in the tomographic images (Grand et al., 1997), and offers a viable process to decouple the surface plate motions with the mantle flow, found by similar models (Becker et al., 2003; Jadamec and Billen, 2010).

Complex mantle flow may have consequences for the interpretation of seismic anisotropy observed at subduction zones. Here, the fast SKS component generally orients parallel to the trench, which is explained by trench-parallel mantle circulation around subducting plates (Long and Silver, 2008; Russo and Silver, 1994). In our models with lateral slab density variations the flow is effectively trench-parallel in just a 30 km thick layer implying that, assuming a sub-parallel lattice preferred orientation (LPO) as it is done routinely by seismologists, it would not produce substantial time delays ($\sim$0.3 s for 5% anisotropic peridotite). However, because anisotropic mantle minerals align preferentially with the maximum stretching directions that coincides with the flow direction only during simple shear deformation (Kaminski and Ribe, 2002), the simple relation between LPO orientation and flow direction is not always warranted, even in the 30 km thick mantle layer with trench-parallel flow. Moreover, in general it is difficult to predict the LPO development in the subslab mantle where deformation is a mixture of different shear and normal strain rate components. In order to make more robust inferences on the resulting seismic anisotropy, an accurate investigation that accounts for the whole deformational history of the mantle is required (Faccenda and Capitanio, 2012).

Nevertheless, the fact that deformation occurs beneath modeled subducting slabs at a depth range of $\sim$100–350 km by simple shear rather than pure shear allows speculations on the LPO development. Under conditions of trench-perpendicular v_y gradients ($v_{y,x}$ and $v_{y,z}$) larger than trench-parallel v_x gradients ($v_{x,y}$ and $v_{x,z}$), the LPO tends to be aligned with the trench. If the opposite occurs the anisotropy should align perpendicular to the trench. In our models with lateral slab buoyancy variations v_y gradients are in general comparable to/larger than v_x, so that the resulting strain ellipsoid should be strongly aligned sub-parallel to the trench. Therefore, model results support a rather general lateral flow component that might increase the trench-parallel anisotropy component at the expense of the trench-perpendicular component. Furthermore, thermal and mechanical (grains-size dependent) rheological weakening feedbacks not considered here act to decrease the coupling between the slab and subslab mantle (Long and Silver, 2009), i.e. the asthenosphere, thus reducing trench-perpendicular flow in the entrained mantle and associated anisotropy.

Faccenda and Capitanio (2012) showed that trench-parallel anisotropy develops beneath relatively narrow plates by pure shear deformation and simultaneous toroidal flow when retreat motions are maximized. In these cases, lateral pressure gradients together with efficient subslab mantle decoupling from the overlying slab may then add to the background toroidal motions yielding trench-parallel LPO orientation consistent with the observed anisotropy patterns.

4.3. Implications for natural subduction zones

We have modeled the slabs negative buoyancy gradients, mimicking similar thickness variations due to lithospheric age variations at trenches. The validity of our outcomes can be extended to other types of integrated buoyancy heterogeneities, whether endogenous to the plates or exogenous.

In the subducting Nazca plate, present-day age at the trench varies from 0, in the north and south plate divergent margins, to $\sim$55 Ma in the center, thus varying from 0 to $\sim$90 km thickness. The resulting Stokes velocity is thus expected to vary accordingly, eventually driving slab deformation and upper plate tectonics (Capitanio et al., 2011). All major subduction zones present similar oceanic lithospheric age-gradients (Sdrolias and Müller, 2006).

Other subducting plate characteristics that have an impact on the slab buoyancy are the nature of the lithopshere, whether oceanic or continental, as well as the depth of subduction, modulating the integrated slab pull. As an example, in the Tonga subduction zone a mature oceanic plate is subducting along the $\sim$2000 km trench. Although no thickness variation can be invoked for this plate older than 80 Ma, towards the south continental lithosphere is subducting in the Kermadec zone (Sdrolias and Müller, 2006). The buoyancy gradients here might be increased by the depth of subduction, reaching the lower mantle beneath the Tonga but not deeper than 300 km beneath Kermadec (Fischer et al., 1991; Lallemand et al., 2005). In this subduction zone, convergence velocity decreases largely from Tonga to Kermadec, from 12 to less than 1 cm yr^{-1}. Although speculative, large trench-parallel velocity gradients together with first order toroidal flow due to the maximized retreat motions (Faccenda and Capitanio, 2012) could explain the trench-parallel subslab seismic anisotropy measured (Long and Silver, 2008).

Typical features such as slab windows and detachments, but also volcanic ridges, might confer slab pull gradients similar to those idealized here, provided they are large enough to alter the slab pull. We have shown that due to the stiffness of slabs, small size buoyancy perturbations might not effectively alter the slab velocity. This is compatible with the global plate motions compilations, where small ridges do not apparently alter the convergence

motions along trenches (DeMets et al., 1990, 2010). Yet, the simplified analysis in a previous section allows inferring that the effect of smaller perturbations should be more evident on smaller and/or younger plates. While in small plates the perturbations have a larger contribution on the average buoyancy, young and thin plates have smaller rigidity, so that perturbation should be more effective in small and young over old and large oceanic plates, resulting in larger deformation in young subducting slabs.

5. Conclusions

Buoyancy heterogeneities in slabs on Earth are primarily a consequence of age-dependent thickness variations along trenches. Three-dimensional numerical models of subduction show that the mantle flow during subduction of heterogeneous plates, along-trench variations of pull forces and sinking rates, trigger mantle flow sub-parallel to the slab. For Earth-like slabs stiffness the trench-parallel component becomes significant only when heterogeneities are wider than $\sim$1000 km, or less in young subducting oceanic lithospheres. The lateral flow component does not largely alter the convection pattern around the slab, however, we found that (1) it introduces large trench-parallel simple shear at depths of $\sim$100–350 km and (2) at a depth of $\sim$200 km trench-parallel flow occurs. In the narrow layer of trench-parallel flow material can be transported over large distance around very wide slabs. Slabs internal deformation decouples the mantle flow from motions at surface, such that on Earth trench and slab motions might not always correspond. Therefore, we propose that heterogeneous subducting lithosphere buoyancy structures are required to explain slabs' convoluted morphologies, second-order plate motions and complex mantle circulation. Thickness variations, as well as slab break offs and windows, variable depth of subduction and continental block entrainment are commonly found along subduction zones. Because these all introduce similar buoyancy heterogeneities along the trenches, complexities as those shown here should have a global presence.

Acknowledgment

Discussions with T.W.Becker and L.N. Moresi are acknowledged. We thank two anonymous reviewers for insightful suggestions. This research was supported by the Australian Research Council *Discovery Projects* DP0987374 and DP110101697 awarded to F.A.C.

Appendix A. Supporting information

Supplementary data associated with this article can be found in the online version at 10.1029/2001GC000222.

References

Afonso, J.C., Ranalli, G., Fernandez, M., 2007. Density structure and buoyancy of the oceanic lithosphere revisited. Geophys. Res. Lett. 34, L10302, http://dx.doi.org/10.1029/2007GL029515.

Becker, T.W., Kellogg, J.B., Ekström, G., O'Connell, R.J., 2003. Comparison of azimuthal seismic anisotropy from surface waves and finite strain from global mantle-circulation models. Geophys. J. Int. 155, 696–714.

Billen, M., Gurnis, M., Simons, M., 2003. Multiscale dynamics of the Tonga–Kermadec subduction zone. Geophys. J. Int. 153, 359–388.

Buttles, J., Olson, P., 1998. A laboratory model for subduction zone anisotropy. Earth Planet. Sci. Lett. 164, 245–262.

Capitanio, F.A., Faccenna, C., Zlotnik, S., Stegman, D.R., 2011. Subduction dynamics and the origin of Andean orogeny and Bolivian Orocline. Nature 480, 83–86, http://dx.doi.org/10.1038/nature10596.

Capitanio, F.A., Morra, G., 2012. The bending mechanics in a dynamic subduction system: constraints from numerical modeling and global compilation analysis. Tectonophysics 522–523, 224–234.

Capitanio, F.A., Morra, G., Goes, S., 2007. Dynamic models of downgoing plate-buoyancy driven subduction: subduction motions and energy dissipation. Earth Planet. Sci. Lett. 262, 284–297.

Capitanio, F.A., Morra, G., Goes, S., Weinberg, R.F., Moresi, L., 2010a. India–Asia convergence driven by the subduction of the Greater Indian continent. Nat. Geosci. 3, 136–139.

Capitanio, F.A., Stegman, D.R., Moresi, L., Sharples, W., 2010b. Upper plate controls on deepsubduction, trenchmigrations and deformations at convergent margins. Tectonophysics 483, 80–92, http://dx.doi.org/10.1016/j.tecto.2009.08.020.

Conrad, C.P., Behn, M.D., Silver, P.G., 2007. Global mantle flow and the development of seismic anisotropy: differences between the oceanic and continental upper mantle. J. Geophys. Res. 112, http://dx.doi.org/10.1029/2006JB004608.

DeMets, C., Gordon, R.G., Argus, D.F., 2010. Geologically current plate motions. Geophys. J. Int. 181, http://dx.doi.org/10.1111/j.1365-246X.2009.04491.x.

DeMets, C., Gordon, R.G., Argus, D.F., Stein, S., 1990. Current plate motions. Geophys. J. Int. 101, 425–478.

Dvorkin, J., Nur, A., Mavko, G., Ben-Avraham, Z., 1993. Narrow subducting slabs and the origin of backarc basins. Tectonophysics 227, 63–79.

Faccenda, M., Capitanio, F.A., 2012. Development of mantle seismic anisotropy during subduction-induced 3-D flow. Geophys. Res. Lett. 39, L11305, http://dx.doi.org/10.1029/2012GL051988.

Fischer, K.M., Creager, K.C., Jordan, T.H., 1991. Mapping the Tonga Slab. J. Geophys. Res. 96, 14403–14427.

Funiciello, F., Faccenna, C., Giardini, D., 2004. Role of lateral mantle flow in the evolution of subduction systems: insights from laboratory experiments. Geophys. J. Int. 157, 1393–1406.

Funiciello, F., Moroni, M., Piromallo, C., Faccenna, C., Cenedese, A., Bui, H.A., 2006. Mapping mantle flow during retreating subduction: laboratory models analyzed by feature tracking. J. Geophys. Res. 111, http://dx.doi.org/10.1029/2005JB003792.

Garfunkel, Z., Anderson, C.A., Schubert, G., 1986. Mantle circulation and the lateral migration of subducted slab. J. Geophys. Res. 91, 7205–7223.

Grand, S.P., van der Hilst, R.D., Widiyantoro, S., 1997. High resolution global tomography: a snapshot of convection in the Earth. Geol. Soc. Am. Today 7, 1–7.

Hall, C.E., Fischer, K.M., Parmentier, E.M., Blackman, D.K., 2000. The influence of plate motions on three-dimensional back arc mantle flow and shear wave splitting. J. Geophys. Res. 105, 28009–28033.

Hoernle, K., Abt, D.L., Fischer, K.M., Nichols, H., Hauff, F., Abers, G.A., van den Bogaard, P., Heydolph, K., Alvarado, G., Protti, M., Strauch, W., 2008. Arc-parallel flow in the mantle wedge beneath Costa Rica and Nicaragua. Nature 451 , http://dx.doi.org/10.1038/nature06550.

Honda, S., Yoshida, T., 2005. Effects of oblique subduction on the 3-D pattern of small-scale convection within the mantle wedge. Geophys. Res. Lett. 31, L13307, http://dx.doi.org/10.1029/2005GL023106.

Iaffaldano, G., Di Giuseppe, E., Corbi, F., Funiciello, F., Faccenna, C., Bunge, H.P., 2012. Varying mechanical coupling along the Andean margin: implications for trench curvature, shortening and topography. Tectonophysics 526–529, 16–23.

Jadamec, M.A., Billen, M., 2010. Reconciling surface plate motions with rapid three-dimensional mantle flow around a slab edge. Nature 465, 338–341.

Kaminski, E., Ribe, N.M., 2002. Timescales for the evolution of seismic anisotropy in mantle flow. Geochem. Geophys. Geosyst. 3, http://dx.doi.org/10.1029/2001GC000222.

Kincaid, C., Griffiths, R.W., 2003. Laboratory models of the thermal evolution of the mantle during rollback subduction. Nature 425, 58–62.

Kneller, E.A., van Keken, P.E., 2007. Trench-parallel flow and seismic anisotropy in the Mariana and Andean subduction systems. Nature 450, http://dx.doi.org/10.1038/nature06429.

Kreemer, C., 2009. Absolute plate motions constrained by shear wave splitting orientations with implications for hot spot motions and mantle flow. J. Geophys. Res. 114, http://dx.doi.org/10.1029/2009JB006416.

Krien, Y., Fleitout, L., 2008. Gravity above subduction zones and forces controlling plate motions. J. Geophys. Res. 113 , http://dx.doi.org/10.1029/2007JB005270.

Lallemand, S., Heuret, A., Boutelier, D., 2005. On the relationships between slab dip, back-arc stress, upper plate absolute motion, and crustal nature in subduction zones. Geochem. Geophys. Geosyst. 6, 917.

Long, M.D., Silver, P.G., 2008. The subduction zone flow field from seismic anisotropy: a global view. Science 319, 315–319.

Long, M.D., Silver, P.G., 2009. Mantle flow insubduction systems: the subslab flow field and implications for mantle dynamics. J. Geophys. Res. 114, 315–319, http://dx.doi.org/10.1029/2008JB006200.

Mehl, L., Hacker, B.R., Hirt, G., Kelemen, P.B., 2003. Arc-parallel flow within the mantle wedge: evidence from the accreted Talkeetna arc, south central Alaska. J. Geophys. Res. 108, http://dx.doi.org/10.1029/2002JB002233.

Miller, M.S., Kenneth, B.L.N., Toy, V.G., 2006. Spatial and temporal evolution of the subducting Pacific plate structure along the western Pacific margin. J. Geophys. Res. 111, http://dx.doi.org/10.1029/2005JB003705.

Moresi, L., Dufour, F., Mülhaus, H.B., 2003. A lagrangian integration point finite element method for large deformation modeling of viscoelastic geomaterials. J. Comput. Phys. 184, 476–497.

Morishige, M., Honda, S., 2011. Three-dimensional structure of P-wave anisotropy in the presence of small-scale convection in the mantle wedge. Geochem. Geophys. Geosyst. 12, Q12010, http://dx.doi.org/10.1029/2011GC003866.
Morra, G., Regenauer-Lieb, K., 2006. A coupled solid-fluid method for modeling subduction. Philos. Mag. 86, 3307–3323.
Morra, G., Regenauer-Lieb, K., Giardini, D., 2006. On the curvature of oceanic arcs. Geology 34, 877–880.
Müller, R.D., Sdrolias, M., Gaina, C., Roest, W.R., 2008. Age, spreading rates, and spreading asymmetry of the world's ocean crust. Geochem. Geophys. Geosyst. 9, Q04006, http://dx.doi.org/10.1029/2007GC001743.
Natarov, S.I., Conrad, C.P., 2012. The role of Poiseuille flow in creating depth-variation of asthenospheric shear. Geophys. J. Int. 191, http://dx.doi.org/10.1111/j.1365-246X.2012.05562.x.
Rodrígues-González, J., Negredo, A.M., Billen, M., 2012. The role of the overriding plate thermal state on slab dip variability and on the occurrence of flat subduction. Geochem. Geophys. Geosyst. 13, Q01002, http://dx.doi.org/10.1029/2011GC003859.
Russo, R.M., Silver, P.G., 1994. Trench-parallel flow beneath the Nazca Plate from seismic anisotropy. Science 263, 1105–1108.
Rychert, C.A., Fischer, K.M., Abers, G.A., Plank, T., Syracuse, E., Protti, J.M., Gonzalez, V., Strauch, W., 2008. Strong along-arc variations in attenuation in the mantle wedge beneath Costa Rica and Nicaragua. Geochem. Geophys. Geosyst. 9, Q10S10, http://dx.doi.org/10.1029/2008GC002040.
Schellart, W.P., 2004. Kinematics of subduction and subduction-induced flow in the upper mantle. J. Geophys. Res. 109, 2970.
Sdrolias, M., Müller, R.D., 2006. Controls on back-arc basin formation. Geochem. Geophys. Geosyst. 7 , http://dx.doi.org/10.1029/2005GC001090.
Sobolev, S.V., Babeyko, A.Y., 2005. What drives orogeny in the Andes? Geology 33, 617–620.
Stadler, G., Gurnis, M., Burstedde, C., Wilcox, L.C., Alisic, L., Ghattas, O., 2010. The dynamics of plate tectonics and mantle flow: from local to global scales. Science 329, 1033–1038.
Stegman, D.R., Freeman, J., Schellart, W.P., Moresi, L., May, D., 2006. Influence of trench width on subduction hinge retreat rates in 3-D models of slab rollback. Geochem. Geophys. Geosyst. 7, 1–22.
Stevenson, D.J., Turner, J.S., 1977. Angle of subduction. Nature 270, 334–336.
Turcotte, D.L., Schubert, G., 1982. Geodynamics, Application of Continuum Mechanics to Geological Problems. John Wiley & Sons, New York.